Draft version November 11, 2015
Preprint typeset using LaTeX style emulateapj v. 11/10/09

arXiv:1411.1454v2 [astro-ph.HE] 10 Nov 2015

# A GENERAL RELATIVISTIC NULL HYPOTHESIS TEST WITH EVENT HORIZON TELESCOPE OBSERVATIONS OF THE BLACK-HOLE SHADOW IN Sgr A*

Dimitrios Psaltis, Feryal Özel, Chi-Kwan Chan, and Daniel P. Marrone
Astronomy Department, University of Arizona, 933 N. Cherry Ave, Tucson, AZ 85721
*Draft version November 11, 2015*

## ABSTRACT

The half opening angle of a Kerr black-hole shadow is always equal to $(5 \pm 0.2)GM/Dc^2$, where $M$ is the mass of the black hole and $D$ is its distance from the Earth. Therefore, measuring the size of a shadow and verifying whether it is within this 4% range constitutes a null hypothesis test of General Relativity. We show that the black hole in the center of the Milky Way, Sgr A*, is the optimal target for performing this test with upcoming observations using the Event Horizon Telescope. We use the results of optical/IR monitoring of stellar orbits to show that the mass-to-distance ratio for Sgr A*is already known to an accuracy of $\sim 4\%$. We investigate our prior knowledge of the properties of the scattering screen between Sgr A* and the Earth, the effects of which will need to be corrected for in order for the black-hole shadow to appear sharp against the background emission. Finally, we explore an edge detection scheme for interferometric data and a pattern matching algorithm based on the Hough/Radon transform and demonstrate that the shadow of the black hole at 1.3 mm can be localized, in principle, to within $\sim 9\%$. All these results suggest that our prior knowledge of the properties of the black hole, of scattering broadening, and of the accretion flow can only limit this General Relativistic null hypothesis test with Event Horizon Telescope observations of Sgr A* to $\lesssim 10\%$.

*Subject headings:* black hole physics – Galaxy: center – accretion, accretion disks – techniques: image processing – scattering

## 1. INTRODUCTION

One of the most remarkable predictions of strong-field gravity is the existence of a region outside a black-hole horizon, in which there are no closed photon orbits. All photons that venture into this region eventually cross the horizon and are removed from the observable Universe. The net result is a shadow imprinted by every black hole on the emission that originates in its vicinity (Bardeen 1973; Luminet 1979).

The size of the shadow of a black hole is determined by the radius of the photon orbit in its spacetime. The radius of the photon orbit changes significantly with black-hole spin, from $3GM/c^2$ for a non-spinning black hole to $GM/c^2$ for a maximally spinning one in Boyer-Lindquist coordinates and for a prograde photon orbit (Bardeen et al. 1972; here $M$ is the mass of the black hole), However, because of gravitational lensing, the size and shape of the black-hole shadow observed at infinity has a very weak dependence on the black-hole spin or the orientation of the observer. Its radius changes from $\sqrt{27} \simeq 5.2\ M$ for a non-spinning black hole (independent of orientation) to $4.84\ M$ for a maximally spinning one viewed pole on (see, e.g., de Vries 2000; Takahashi 2004; Bozza et al. 2006; Johannsen & Psaltis 2010; Chan et al. 2013). As a result, for a black hole of known mass and distance, identifying the presence of the shadow and confirming that its size is in the narrow range $(4.8 - 5.2)\ M$ constitutes a null hypothesis test of the Kerr metric. Indeed, for other plausible black-hole or naked-singularity metrics the size of the shadow has been shown to be significantly different (for different modifications to the Kerr metric see, e.g., Bambi & Freese 2009; Johannsen & Psaltis 2010; Bambi & Yoshida 2010; Amarilla & Eiroa 2013).

Current 1.3 mm VLBI observations of the black hole in the center of the Milky Way, Sgr A*, (Doeleman et al. 2008; Fish et al. 2009, 2014) and earlier theoretical expectations (e.g., Falcke et al. 2000; Özel et al. 2000) all but ensure that upcoming observations with the complete Event Horizon Telescope (EHT) will generate horizon-scale images of its accretion flow and of the black-hole shadow (see, e.g., numerical simulations of Broderick et al. 2009, 2011; Dexter et al. 2009, 2010; Mościbrodzka et al. 2009, 2013, 2014; Chan et al. 2015a). In this article, we explore the prospect of performing the general relativistic null hypothesis test discussed above using the upcoming EHT observations of Sgr A*. In this initial study, we investigate the various systematic uncertainties that arise from our incomplete prior knowledge of the properties of the black-hole, of the intervening medium between the Galactic Center and the Earth, and of the astrophysical complexities that affect the measurement of the size of the black-hole shadow. With these uncertainties under control, we will then be able to assess, in future work, the scatter that is introduced by the inherent uncertainties in the measurements, the incomplete coverage of the interferometric $u - v$ plane by the EHT array, and the particular algorithms for image reconstruction that will be employed.

In §2, we investigate our prior knowledge of the mass $M$ of Sgr A* and its distance $D$ from Earth, the ratio of which determines the apparent size of the black-hole shadow on the sky. We show that currently available models of the orbits of nearby stars developed by two groups using observations with Keck (Ghez et al. 2008; Boehle et al. 2015) and with the VLT (Gillessen et al. 2009a, 2009b) give consistent results and constrain the

ratio $M/D$ to within $\simeq 4\%$. This accuracy will only improve with next generation adaptive optics systems on 30-m class telescopes (Weinberg et al. 2005), with interferometric observations of stellar orbits (Eisenhauer et al. 2011), or with the discovery of a radio pulsar in orbit around the black hole (Pfahl & Loeb 2004; Liu et al. 2012; Psaltis et al. 2015b).

In §3, we study the inferred properties of the scattering screen between the Earth and the Galactic Center that blurs the image of the shadow. As demonstrated in Fish et al. (2014), blurring due to scattering takes place in the ensemble average regime (see Narayan & Goodman 1989; Goodman & Narayan 1989). As a result, the blurring effects on the image can be formally corrected for, if the scattering kernel at 1.3 mm is known *a priori*. After collecting all the published measurements of the scattered broadened image of Sgr A$^*$, we find that different aspects of the scattering ellipse at longer wavelengths can be inferred with a fractional accuracy in the range $3-20\%$. We argue that extrapolating these results down to the 1.3 mm wavelength of the EHT observations requires a more accurate measurement of the long-wavelength scattering kernel as well as a better understanding of the wavelength dependence of its anisotropy.

Finally, in §4 we investigate model independent methods to measure the shape and size of the black-hole shadow from interferometric observations. We explore an edge detection algorithm based on the gradient of the image brightness that allows us to extract the shape of the shadow from the image and a pattern matching algorithm based on the Hough/Radon transform to measure the shadow properties. We apply these algorithms to our recent ray tracing calculation of GRMHD simulations and find that, in principle, the shape and size of the black-hole shadow can be measured to a $\sim 9\%$ accuracy.

## 2. THE APPARENT SIZE OF THE BLACK-HOLE SHADOW

General relativity predicts the size of a black-hole shadow in units of the gravitational radius $GM/c^2$, which we will denote hereafter simply as $M$. However, in order to compare the theoretical predictions to the observations, we need a prior knowledge of the ratio $M/D$ of the mass of the black hole to its distance from Earth. This ratio sets the angular size of one gravitational radius on the sky of an observer.

The mass of Sgr A$^*$ and its distance from the Earth can be inferred by fitting Keplerian orbits to optical/IR observations of stars in the vicinity of the black hole (see, e.g., Ghez et al. 2008; Gillessen et al. 2009a, 2009b). These measurement are typically highly correlated. Astrometric observations of the stellar positions typically constrain the ratio $M/D^3$, whereas spectral measurements of radial velocities constrain the ratio $M/D$. When multiple such data sets are combined, the correlated errors between mass and distance stretch along the curve $M \sim D^2$.

In general, each study of the stellar orbits around Sgr A$^*$ leads to the two-dimensional posterior likelihood $P(D,M)dDdM$. For our purposes, we are only interested in the marginalized posterior likelihood over the ratio $P(M/D)d(M/D)$. If we set $\theta \equiv M/D$ such that

$$\left|\frac{d\theta}{dD}\right| = \frac{M}{D^2} \qquad (1)$$

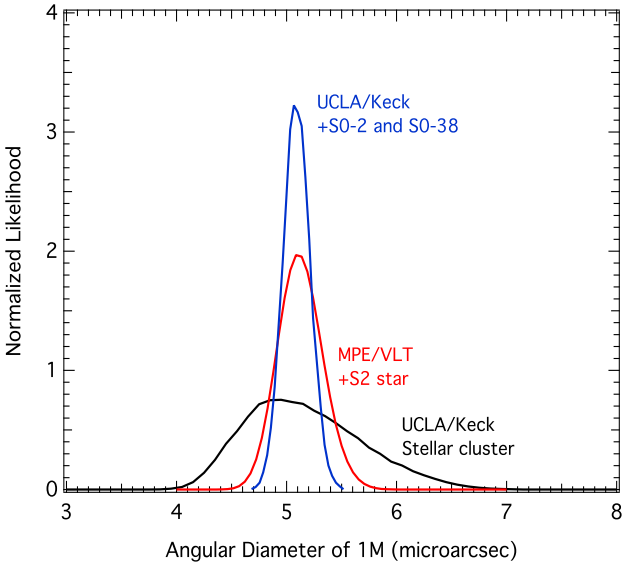


FIG. 1.— The posterior likelihood of the angular size of one gravitational radius (i.e., $GM/c^2D$) for Sgr A$^*$, as inferred from fitting Keplerian orbits to astrometric observations of S stars. The black curve shows the result of a UCLA/Keck study, in which only the astrometric observations of the inner stellar cluster were considered (Ghez et al. 2008). The red curve shows the result of an MPE/VLT study, in which the radial velocities of the S2 star were also incorporated (Gillessen et al. 2009a, 2009b). The blue curves shows the result of the most recent UCLA/Keck study, which also employs data for the S0-38 star (Boehle et al. 2015). The posterior likelihood in the Boehle et al. (2015) analysis corresponds to an angular size of one gravitational radius that is equal to 5.09±0.17 $\mu$arcsec.

and

$$P(\theta,M)d\theta dM = P(D,M)dDdM \qquad (2)$$

then we conclude that

$$P(\theta)d\theta = \int_M P(\theta,M)dMd\theta = \int_M \frac{D^2}{M}P(D,M)dMd\theta\ , \qquad (3)$$

Using the two-dimensional posterior likelihood $P(D,M)$ over the distance and the mass of the black hole from studies of stellar orbits, we can employ this equation to calculate the posterior likelihood over the angular size of one gravitational radius for Sgr A$^*$.

Figure 1 shows the improvement in the inference of this angular size, as increasingly more data are incorporated for the stellar orbits. When only the astrometric orbits of the inner stellar cluster are considered (i.e., using the two-dimensional posterior likelihoods $P(D,M)$ shown in Figure 11 of Ghez et al. 2008), the uncertainty in the angular size of Sgr A$^*$ is at the 10% level. When radial velocity data for the S2 star are also incorporated (i.e., using the equivalent of Figure 15 of Gillessen et al. 2009b but including the data for the S2 orbit, as discussed in Gillessen et al. 2009a), the angular size of one gravitational radius for Sgr A$^*$ becomes 5.12±0.29 $\mu$arcsec. Finally, when the data for the S0-38 orbit are also included (Boehle et al. 2015), then the angular size of one gravitational radius becomres equal to 5.09±0.17 $\mu$arcsec. This $\sim 3-4\%$ uncertainty in the last measurement is comparable to the ±4% uncertainty in the predicted size of the black-hole shadow given that we currently do not have a prior knowledge of the spin of the black hole or of the orientation of its spin axis with respect to the Earth.

A number of different observations in the near future will reduce significantly the uncertainties in the above measurements. Next generation adaptive optics systems operating in 30-m class telescopes may discover stars with orbits that are closer to the black hole than the currently known S stars and that display different relativistic effects. The improved accuracy of the astrometric measurements and the detection of relativistic precession will lead to uncertainties in the inferred mass of Sgr A* and its distance that are as small as 0.1% (Weinberg et al. 2005). At the same time, the detection of even a single radio pulsar in a sub-year orbit around Sgr A* will lead to an unprecedentent fractional accuracy in the measurement of the black-hole mass and distance that may be as low as $10^{-6}$ (Liu et al. 2012; see also Pfahl & Loeb 2004; Psaltis et al. 2015b).

## 3. THE SCATTERING SCREEN

The long-wavelength images of Sgr A* are much larger than expected for the emission from the accretion flow and their size depends on wavelength in a manner that is consistent with their being scatter-broadened by the interstellar medium (see Figure 2, Bower et al. 2006, and references below). At the 1.3 mm wavelength of the EHT observations, the size of the scattering Kernel is expected to be of the order of 22 $\mu$arcsec, which is approximately one fourth of the size of the black-hole shadow. The effect of scattering is to smooth the underlying image structure at scales smaller than the size of the Kernel, potentially masking and blurring the edges of the shadow.

Fish et al. (2014) argued that scatter broadening towards Sgr A* takes place in the ensemble average regime (Narayan & Goodman 1989; Goodman & Narayan 1989) and is, therefore, deterministic. Recent observations of refractive substructure at larger wavelengths (Gwinn et al. 2014), however, clearly suggest that the averaging over the scattering ensemble is incomplete and a subsequent theoretical study (Johnson & Gwinn 2015) demonstrated that this substructure is not quenched by the presence of an extended source. Nevertheless, if data from many epochs and hence from many realizations of the scattering ensemble are added, the effect of scatter broadening can be considered as taking place in the ensemble average regime.

Formally speaking, scatter broadening in this regime causes the amplitudes of the observed interferometric visibilities to be reduced by a real factor that is equal to the Fourier transform of the scattering kernel. If we have good prior knowledge of the scattering kernel, we can then easily correct for the blurring effects of scattering. Fish et al. (2014) explored different avenues of deblurring (direct or with Wiener filters) and demonstrated their efficiency with mock EHT data. They also considered the formal uncertainties in the measurement of the scattering kernel properties (as reported by Bower et al. 2006) and their effect on the results of the deblurring algorithms.

In this section, we explore the systematic uncertainties in the measurements of the properties of the scattering kernel. This is important for a number of reasons, which we discuss below.

Measurements of the scattering kernel properties need to be done at relatively long wavelengths, for which the size of the source is much smaller than the size of the kernel. Recent observations found evidence for milliarcsec substructure in the images of Sgr A* at wavelengths as large as 1.3 cm (Gwinn et al. 2014). This is corroborated by the measured deviation of the wavelength dependence of the scattering kernel from the theoretical expected scaling of $\lambda^2$ at comparable wavelengths, as we show in Figure 3 below (see also Falcke & Markoff 2012). As a result, the properties of the scattering kernel need to be measured at wavelengths as large as $10 - 20$ cm and then extrapolated down to the 1.3 mm wavelength of the EHT. This extrapolation by two orders of magnitude runs the risk of amplifying even minor systematic errors that are unaccounted for.

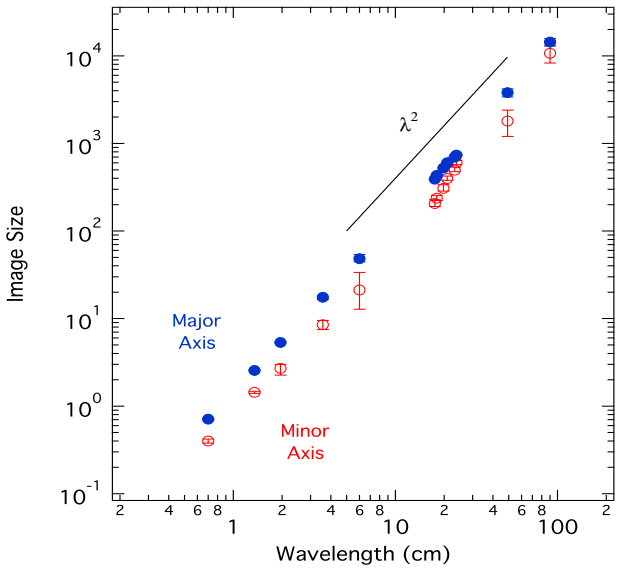


FIG. 2.— The observed dependence on wavelength of the major and minor axis dimensions of the scatter broadened image of Sgr A*. The solid black line shows the expected $\lambda^2$ dependence.

The large dynamical range of the extrapolation becomes even more important when we consider the fact that the measured scattering kernel towards Sgr A* is highly anisotropic. It is often modeled in terms of an ellipse, with a 2:1 axis ratio and a major axis that is oriented primarily along the E-W axis on the sky (see §3.1 below). The origin of the anisotropy is widely believed to be related to large scale magnetic fields in the turbulent interstellar medium, the statistical properties of which determine both the axis ratio of the scattering ellipse and its orientation (see, e.g., Chandran & Backer 2002). These two quantities may not remain constant, as is currently assumed, when the wavelength changes by over two orders of magnitude. A theoretical investigation of this issue is necessary to make progress but is beyond the scope of the present work.

Our goal in this section is to explore the wavelength dependence of the properties of the scattering kernel towards Sgr A* and infer the level of existing systematic differences between the various measurements across the mm-to-cm spectrum.

### 3.1. *Observational Constraints*

Tables 1-3 summarize the published measurements of the image size of Sgr A* in the mm-to-cm range, for which the data quality was sufficient to detect an elliptical (as opposed to a circular) image. We only consider measurements at wavelengths larger than 0.7 mm,

as source structure is clearly seen at 1.3 and 3 mm (Doeleman et al. 200; Bower et al. 2014). For most wavelengths, there has been only one measurement reported, which is what we include. For some wavelengths, more than one measurements have been carried out; in these cases, as we explain below, we chose the result of the most recent publication (when the same data were analyzed more than once) or the one with the smallest reported uncertainties (which is often the most recent, as well).

In particular:
*(i)* At 20.9 cm, we chose the measurement reported in Bower et al. (2006), as opposed to the one in Yusef-Zadeh et al. (1994), because the latter has a very large reported uncertainty in the measurement of the minor axis of the ellipse.
*(ii)* At 3.5 cm, six measurements have been reported: Lo et al. (1985), Jauncey et al. (1989), Lo et al. (1993), Bower et al. (2004), Shen et al. (2005; this study included analysis of all previous VLBA observations between 1994 and 2004) and Bower et al. (2014); all of these results are statistically consistent with each other. we chose the measurement reported in Shen et al. (2005) as representative for this wavelength.
*(iii)* At 2 cm, we chose the measurement reported in Shen et al. (2005), as opposed to the one in Bower et al. (2004), because of the large uncertainty in the measurement of the size of the minor axis in the latter study.
*(iv)* At 1.35 cm, five measurements have been reported: Lo et al. (1993), Alberdi et al. (1993; which were analyzed again by Marcaide et al. 1999 to correct an error), Bower et al. (2004), Shen et al. (2005; this study included analysis of all previous VLBA observations between 1994 and 2004), and Lu et al. (2011). In the last study, 10 individual measurements were obtained over the course of 10 days. The results of these measurements are listed in Table 2 and, for each quantity, they are statistically consistent with each other. We combined them, according to the method discussed in Appendix A, assuming that they are all drawn from the same underlying $\delta$-function distribution. We obtained $2.56 \pm 0.01$ marcsec, $1.44 \pm 0.04$ marcsec and $79.5 \pm 0.4^\circ$ as the most likely values of the major axis, minor axis, and position angle, respectively. These values are consistent with the earlier, less accurate results of Lo et al. (1993), Marcaide et al. (1999), Bower et al. (2004) and Shen et al. (2005).
*(v)* At 0.7 cm, four sets of measurements have been reported: Bower et al. (2004), Shen et al. (2005), Lu et al. (2011), and Akiyama et al. (2013). All measurements are statistically consistent with each other. However, since each data set comprises several (up to 10) observations each, it remains a possibility that, when the data from each study are statistically combined, as described in Appendix A, then systematic differences between studies will be revealed. In order to explore this, we focused on the studies of Shen et al. (2005) and Lu et al. (2011) and combined the data assuming that, for each study, all measurements were drawn from the same underlying $\delta$-function distribution. For the measurements of Shen et al. (2005), we obtained $0.722 \pm 0.002$ marcsec, $0.398 \pm 0.014$ marcsec, and $80.0 \pm 0.6^\circ$ for the major axis, minor axis, and position angle, respectively. For the measurements of Lu et al. (2011), we obtained $0.713 \pm 0.004$ marcsec, $0.399 \pm 0.021$ marcsec, and $82.0 \pm 0.6^\circ$ for the same quantities. Both sets of measurements are statistically consistent with each other, with similar uncertainties. Even though we will not be using measurements at this wavelength to quantify the degree of scattering in the image of Sgr A$^*$, we will display in the following figures the results obtained from the measurements of Lu et al. (2011).

Of the various measurements included in Table 1, those of Bower et al. (2004, 2006) were performed using closure amplitude techniques, whereas the remaining followed the standard self-calibration approach. The latter was criticized by Bower et al. (2014) as being heavily dependent on the input model, underestimating true errors. This might be explain the fact that the various measurements are often not statistically consistent with each other. However, in our inference of the systematic uncertainties in our prior knowledge of the scattering screen, we use predominantly the measurements performed using closure amplitude techniques.

Figure 2 shows the observed dependence on wavelength of both the major and minor axis dimensions of the scattering ellipse towards Sgr A$^*$. As expected, they both show roughly a $\lambda^2$ scaling. In order to quantify this behavior and infer the level of systematic uncertainties in the measurements, the left panels in Figure 3 show the ratio of the measured major and minor axes of the scattering ellipse to the square of the wavelength of each observation as well as the position angle of the ellipse as a function of wavelength. It is clear from these figures that the various measurements are not statistically consistent with each other, with a level of systematic uncertainty that is larger than the reported formal uncertainties.

It is well understood that, at short wavelengths, the deviation of the scattering law from the expected $\lambda^2$ dependence is caused by the fact that the intrinsic size of Sgr A$^*$ is comparable to or larger than that of the scattering ellipse. On the other hand, at the largest wavelengths, the size of the scattering ellipse is so large that the image of Sgr A$^*$ is blurred together with that of the surrounding emission that has significant structure.

The first goal of this exercise is to identify a dynamical range of wavelengths in which the ratio of the major or minor axis to the square of wavelength remains approximately constant. Figure 3 demonstrates that finding such a range is rather non trivial. In order to make progress, we chose to use the measurements with wavelengths in the range 3 cm$< \lambda <$30 cm and assign any deviation from the expected $\lambda^2$ dependence to the budget of systematic errors.

We combined the data in this wavelength range using the procedure discussed in Appendix A. We assumed that all the measurements of each property (i.e., the major axis, the minor axis, and the position angle) were drawn from a Gaussian distribution, the widths of which quantifies the degree of systematic uncertainties. We then obtained the posterior likelihoods over the centroid and dispersion of each Gaussian, which allow us to quantify the most likely value and the systematic errors in each measurement. The results are shown in the right panels of Figure 3. It is important to emphasize here that the sizes of the two axes and the position angles of the ellipse are not independent measurements. However, due to absence of additional information that would allow us to quantify the degree of correlation between the two measurements, we assumed that they are independent in

TABLE 1
Elliptical Image Sizes of Sgr A*

| Wavelength (cm) | Major Axis (marcsec) | Minor Axis (marcsec) | P.A.[a] (degrees) | Reference |
|---|---|---|---|---|
| 90 | 14400±1400 | 10700±2400 | 95±25 | An et al. 2005 |
| 49.16 | 3800±400 | 1800±600 | 93±4 | Roy & Pramesh Rao 2003 |
| 23.8 | $734.7^{+8.7}_{-5.9}$ | $602.4^{+36.0}_{-29.9}$ | $97.7^{+1.1}_{-7.5}$ | Bower et al. 2006 |
| 23.2 | $697.1^{+5.4}_{-5.9}$ | $496.3^{+40.1}_{-19.6}$ | $76.5^{+2.7}_{-2.1}$ | Bower et al. 2006 |
| 20.9 | $601.8^{+6.0}_{-8.6}$ | $397.3^{+27.2}_{-19.1}$ | $66.1^{+3.9}_{-2.9}$ | Bower et al. 2006 |
| 19.8 | $522.8^{+6.3}_{-8.0}$ | $306.6^{+31.2}_{-21.1}$ | $70.5^{+3.7}_{-2.7}$ | Bower et al. 2006 |
| 18 | $430.8^{+1.9}_{-2.8}$ | $236.7^{+18.6}_{-14.4}$ | $74.9^{+1.8}_{-1.3}$ | Bower et al. 2006 |
| 17.5 | $391.2^{+2.4}_{-3.0}$ | $206.3^{+21.6}_{-15.5}$ | $74.5^{+2.1}_{-1.5}$ | Bower et al. 2006 |
| 6 | $48.4^{+1.9}_{-1.2}$ | $21.2^{+4.2}_{-2.8}$ | $83.2^{+3,4}_{-3.5}$ | Bower et al. 2004[b] |
| 3.56 | $17.5^{+0.5}_{-1.0}$ | $8.5^{+1.0}_{-1.0}$ | $87^{+3}_{-3}$ | Shen et al. 2005 |
| 1.95 | $5.33^{+0.07}_{-0.07}$ | $2.7^{+0.3}_{-0.44}$ | $83^{+3}_{-3}$ | Shen et al. 2005 |
| 1.35 | 2.56±0.01 | 1.44±0.04 | 79.5±0.4 | Lu et al. 2011 |
| 0.7 | 0.722±0.004 | 0.40±0.02 | 82.0±0.6 | Lu et al. 2011 |

[a] Position angle of the major axis, measured in degrees East of North.
[b] The uncertainties displayed here are 1/3 of the $3\sigma$ uncertainties quoted in this reference.

TABLE 2
Elliptical Image Sizes of Sgr A* reported by Lu et al. 2011

| Wavelength (cm) | Major Axis (marcsec) | Minor Axis (marcsec) | P.A.[a] (degrees) |
|---|---|---|---|
| 1.35 | 2.56±0.03 | 1.51±0.10 | 78.6±1.7 |
| | 2.55±0.06 | 1.28±0.08 | 82.0±1.1 |
| | 2.55±0.04 | 1.61±0.13 | 78.0±1.7 |
| | 2.56±0.05 | 1.54±0.08 | 79.8±1.0 |
| | 2.53±0.03 | 1.44±0.05 | 79.6±1.3 |
| | 2.53±0.02 | 1.34±0.05 | 80.2±1.3 |
| | 2.58±0.02 | 1.57±0.05 | 77.2±0.8 |
| | 2.56±0.03 | 1.48±0.05 | 78.9±0.5 |
| | 2.55±0.03 | 1.38±0.10 | 80.7±0.8 |
| | 2.57±0.01 | 1.39±0.05 | 81.1±0.9 |
| 0.7 | 0.71±0.01 | 0.41±0.04 | 81.7±2.3 |
| | 0.72±0.01 | 0.38±0.03 | 82.1±0.8 |
| | 0.72±0.01 | 0.45±0.04 | 82.0±2.4 |
| | 0.71±0.01 | 0.38±0.06 | 84.1±1.1 |
| | 0.71±0.01 | 0.36±0.04 | 84.7±3.1 |
| | 0.72±0.01 | 0.39±0.04 | 80.4±1.6 |
| | 0.72±0.01 | 0.44±0.04 | 81.8±3.1 |
| | 0.72±0.01 | 0.48±0.04 | 78.5±1.3 |
| | 0.72±0.01 | 0.39±0.04 | 81.2±1.3 |
| | 0.68±0.01 | 0.33±0.04 | 86.6±2.1 |

[a] Position angle of the major axis, measured in degrees East of North.

TABLE 3
Elliptical Image Sizes of Sgr A* at 7 mm reported by Shen et al. 2005

| Wavelength (cm) | Major Axis (marcsec) | Minor Axis (marcsec) | P.A.[a] (degrees) |
|---|---|---|---|
| 0.694 | $0.71^{+0.01}_{-0.01}$ | $0.42^{+0.05}_{-0.05}$ | $74^{+2}_{-2}$ |
| 0.695 | $0.722^{+0.002}_{-0.002}$ | $0.395^{+0.019}_{-0.020}$ | $80.4^{+0.8}_{-0.8}$ |
| 0.695 | $0.725^{+0.002}_{-0.002}$ | $0.372^{+0.020}_{-0.018}$ | $80.4^{+0.6}_{-0.9}$ |
| 0.695 | $0.72^{+0.01}_{-0.01}$ | $0.39^{+0.07}_{-0.07}$ | $78^{+2}_{-2}$ |
| 0.695 | $0.72^{+0.01}_{-0.01}$ | $0.42^{+0.03}_{-0.03}$ | $79^{+1}_{-1}$ |
| 0.695 | $0.69^{+0.01}_{-0.01}$ | $0.33^{+0.04}_{-0.04}$ | $83^{+1}_{-1}$ |
| 0.695 | $0.71^{+0.01}_{-0.01}$ | $0.44^{+0.02}_{-0.02}$ | $79^{+1}_{-1}$ |

[a] Position angle of the major axis, measured in degrees East of North.

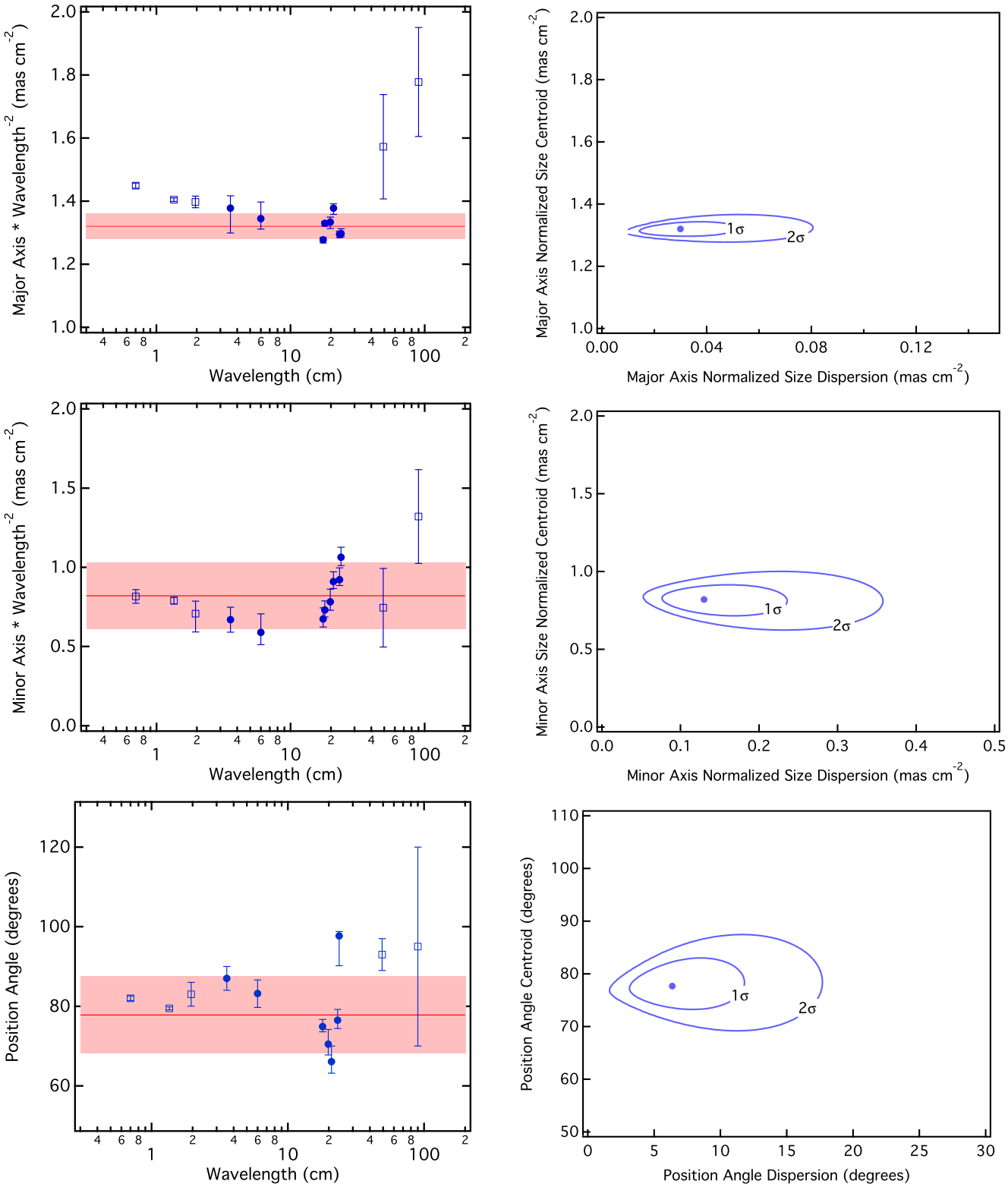


FIG. 3.— *(Left)* The ratio of the measured *(Top)* major axis and *(Middle)* minor axis to the square of the wavelength, as a function of the observed wavelength. *(Bottom)* The position angle of the scattering ellipse, as a function of the observed wavelength. In each panel, the filled circles denote the data points that were used in inferring the average properties of the scattering screen; the colored bands show the 68% posterior likelihood range of parameters of the scattering screen. *(Right)* The 2-dimensional posterior likelihoods of the three parameters shown on the left panels. In all three cases, the systematic uncertainties are assumed to be described by a Gaussian distribution with a given centroid (plotted along the y-axis) and dispersion (plotted along the x-axis). The most likely value of the centroid and dispersion are denoted by a filled circle in each panel, whereas the 68% and 95% contours are also shown as continuous lines.

this statistical study (Bower et al. 2004 and Bower et al. 2014 performed a detailed analysis of the correlated uncertainties for some of the wavelengths used here).

As expected from the visual inspection of the left panels of Figure 3, the inferred dispersions of the three Gaussians are not consistent with zero, indicating the presence of significant systematic uncertainties. Marginalizing over the two-dimensional likelihoods shown in the right panels of Figure 3, as discussed in Appendix A, leads to the following measurement of the properties of the scattering ellipse towards Sgr A*:

$$\begin{aligned}\frac{\text{major axis size}}{\lambda^2} &= 1.32 \pm 0.04 \ \frac{\text{marcsec}}{\text{cm}^2} \\ \frac{\text{minor axis size}}{\lambda^2} &= 0.82 \pm 0.21 \ \frac{\text{marcsec}}{\text{cm}^2} \\ \text{P.A.} &= 77.8 \pm 9.7 \text{ degrees} . \end{aligned} \quad (4)$$

The fractional uncertainties in the inferred size of the major axis of the scattering ellipse is only $\simeq 3\%$. However, the fractional uncertainties in the minor axis size and in the position angle are $\sim 25\%$ and $\sim 12\%$, respectively. The primary reason for these large uncertainties is the fact that most measurements were done with interferometric arrays that have a good coverage along the E-W orientation but a poor coverage perpendicular to it. Additional observations with better coverage in the $N-S$ orientation and a theoretical understanding of the wavelength dependence of the axis ratio and the position angle of the scattering ellipse will be crucial in reducing the level of these systematic uncertainties.

## 4. MEASURING THE PROPERTIES OF THE BLACK-HOLE SHADOW

In its original conception, the black-hole shadow was calculated under the assumption of back illumination of a black hole by a bundle of photons in parallel trajectories that originated in the far infinity (Bardeen 1973). In this case, the trajectories of photons that enter inside the photon radius are gravitationally bent towards the black-hole horizon and never reach the distant observer.

In the realistic case of a mm image of an accreting black hole, such as Sgr A*, the situation is, of course, different, because the majority of photons originate very close to the location of the photon orbit, in all directions. Nevertheless, if the emission is optically thin, as it is expected to be at mm wavelengths for Sgr A*, simulations have repeatedly shown that a shadow will be imprinted on the image of the accretion flow, (see, e.g., Jaroszynski & Kurpiewski 1997; Falcke et al. 2000; Broderick et al. 2009, 2011; Dexter et al. 2009, 2010; Mościbrodzka et al. 2009, 2013, 2014; Chan et al. 2015a). Within the shadow, the brightness of the image is suppressed by at least an order of magnitude, while the outline of the shadow is surrounded by a bright photon ring (see Figure 4).

In principle, comparing a detailed model for the emission properties of the accretion flow around Sgr A* to EHT observations will lead to a measurement of the size and shape of the shadow imprinted by the black hole. However, predicting the details of the brightness profile of the image of the accretion flow that surrounds the black-hole shadow beyond its gross properties is not feasible for two reasons.

The first reason is related to our current understanding of accretion physics. In all available analytical and numerical models of the Sgr A* emission, the thermodynamic properties of the electrons are incorporated in a highly simplified and *ad hoc* fashion (see, e.g., all the references cited above). Quantities such as the energy distribution of electrons and the ratio of electron to ion temperatures are often taken to be constant in time and across different regions of the accretion flow, even though neither of the two assumptions are expected to be correct in detail.

The second reason is related to the expected and observed variability of the emission from Sgr A*. The inner accretion flow is by its nature highly turbulent and variable. As a result, even if we had a highly predictive model for the thermodynamic properties of the plasma, it would still be extremely unlikely that any realization of the model would match the details of any particular snapshot of the observations (Chan et al. 2015b). This would be equivalent to having a model of cloud formation in the Earth's atmosphere and trying to fit cloud shapes to pictures of the sky.

Because of these two reasons, inferring the properties of the black-hole shadow as a by-product of fitting accretion flow images to the EHT observations is not expected to be accurate. Any naive posterior likelihood analysis will direct the model parameters towards minimizing the variance between the observations and the incomplete models in the high intensity regions of the image and not towards accurately reproducing the shape and size of the black-hole shadow.

Our goal here is to study null-hypothesis tests of modified gravity with EHT observations of the black-hole shadow around Sgr A*. In order to achieve this, we need a procedure to analyze the EHT data that focuses on measuring directly the properties of the shadow in a manner that is not seriously affected by our inability to predict the brightness profile of the rest of the image. Indeed, the shape and size of the black-hole shadow depend only on the properties of the spacetime and can be predicted to very high accuracy without being affected by the complexities of modeling the accretion flow. (This is true unless the shadow is completely obscurred by intervening plasma or there is no background emission in the accretion flow on which the shadow can be cast.) As discussed in detail below, the expected sharpness of the shadow allows us to devise a procedure to measure accurately the properties of the shadow is based on edge-detection schemes in image processing.

The sharpness of the shadow, i.e., the length scale over which the image brightness declines, depends primarily on the profile of photon emission within the flow and the velocity field. In order to explore realistic profiles of the emission across the black-hole shadow, we use the results of recent ray-tracing calculations on GRMHD simulations reported in Chan et al. (2015a). The parameters of these models were chosen so that model predictions agree with the spectroscopic measurements and the 1.3 mm image size of Sgr A*. In Chan et al. (2015a), we identified five successful models with different black-hole spins, orientations of the observer, and physical assumptions for the thermodynamic state of the plasma in the accretion flow and in the jet. As a working example, we first use here the results of the `a9SANE` simulation that corresponds to a black hole spinning at 90% of the max-

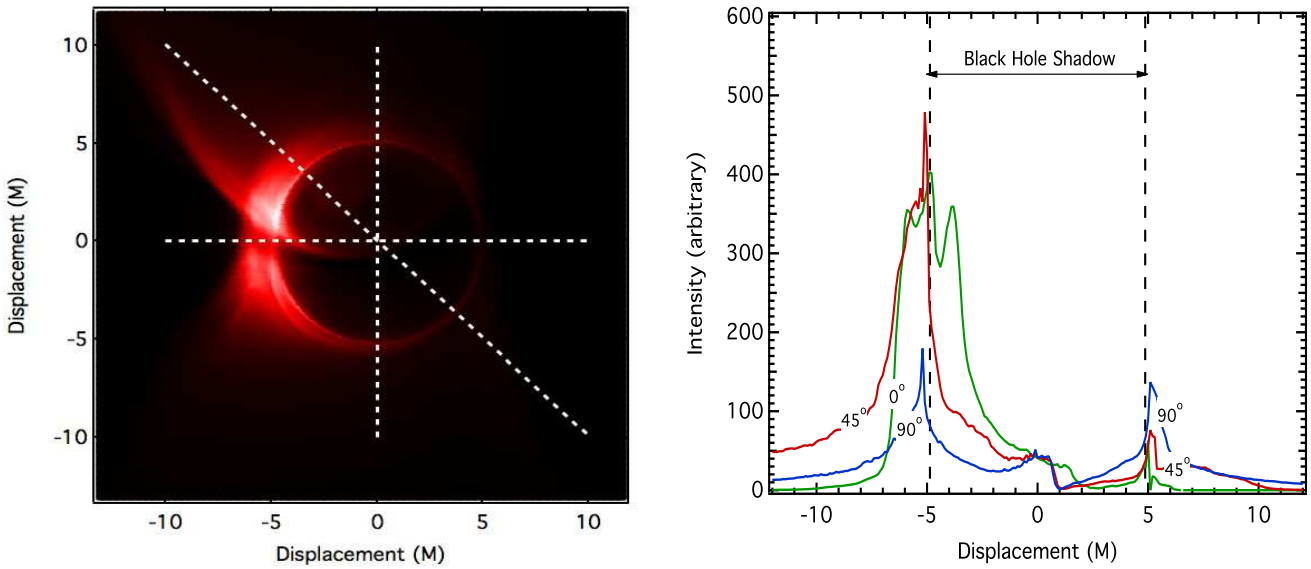


FIG. 4.— *(Left)* A simulated 1.3 mm image of Sgr A*, as calculated from a GRMHD simulation of accretion onto a black hole with spin $a = 0.9$ (`a9SANE` simulation of Chan et al. 2015a). The inclination of the observer is set to 60° with respect to the angular momentum vector of the accretion flow and the thermodynamic parameters of the flow were chosen such that the simulated spectrum is consistent with observations. The three dotted lines show three cross sections at 0°, 45°, and 90° with respect to the equatorial plane. *(Right)* The brightness of the image shown on the left panel, along the three indicated cross sections. In all cases, the rim of the black-hole shadow corresponds to a sharp drop in the brightness. Along most cross sections, the brightness drops from its maximum value at $\sim +0.5$ M outside the nominal location of the shadow to its minimum at $\sim -0.5$ M inside it. Only along the near-equatorial cross sections towards the Doppler boosted part of the emission (center left on the left image), is the transition across the shadow significantly smoother because of the larger emissivity of the intervening accretion flow.

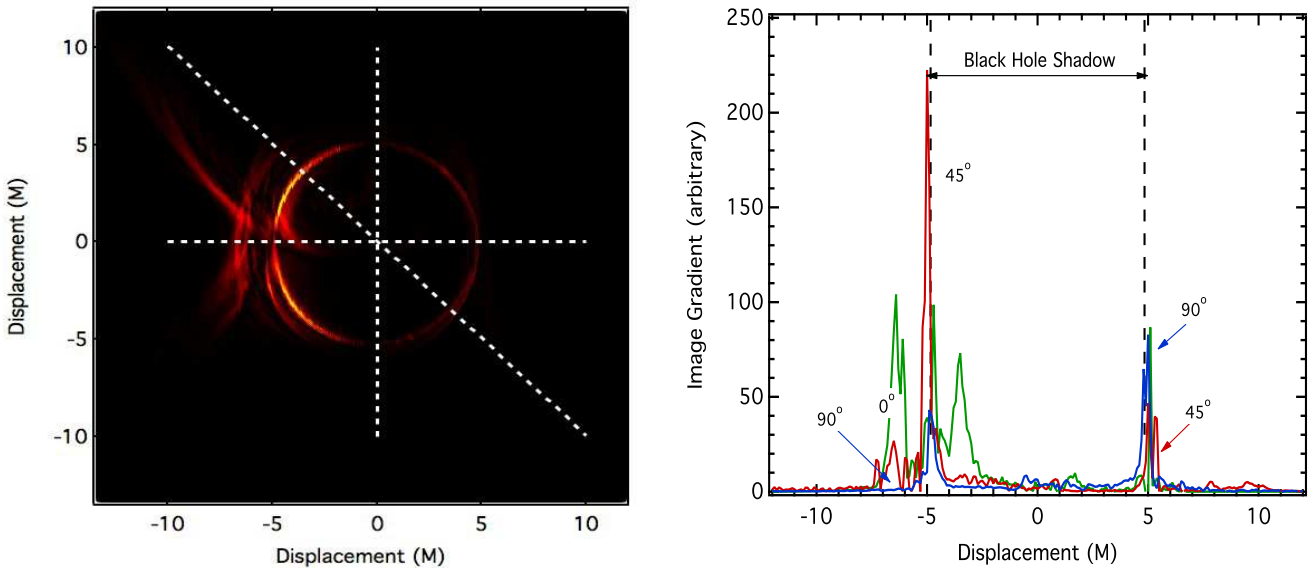


FIG. 5.— *(Left)* A map of the magnitude of the gradient of the image brightness shown in Figure 4. The bright rim at the location of the black-hole shadow is clearly visible. The three dotted lines show three cross sections at 0°, 45°, and 90° with respect to the equatorial plane. *(Right)* The magnitude of the gradient of the image brightness shown on the left panel, along the three indicated cross sections. In almost all cross sections towards the Doppler boosted part of the emission (center left on the left image), the gradient shows a prominent peak within $\sim 0.25$ M of the location of the black-hole shadow. In the opposite side of the image, the gradients are more sharply peaked at displacements that are indistinguishable from the location of the black-hole shadow.

imum spin rate, observed at 60° from its spin axis (see Chan et al. 2015a for a more detailed discussion of this and other similar simulations and Psaltis et al. 2015a for the choice of parameters).

As Figure 4 shows, the rim of the shadow is not sharp at the equatorial plane of the accretion flow—where there is significant emission originating in the front side of the black hole—and towards the Doppler boosted part of the emission. On the other hand, the rim is significantly sharper away from the equatorial plane and towards the Doppler deboosted part of the emission, with the brightness of the image dropping from its maximum to its minimum value over a displacement of $\lesssim 1$ M, producing a well defined edge.

There exist several techniques in image processing for detecting sharp features (edges) in a model-independent fashion. Of these, two algorithms are particularly well suited for images obtained with interferometers: gradient methods (e.g., Marr & Hildreth 1980; Canny 1983) and phase congruency methods (e.g., Kovesi 1999). The gradient method has already been applied successfully to interferometric images to quantify the properties of the turbulent structure of the interstellar magnetic field (Gaensler et al. 2011). We will discuss here the gradient method and explore the phase congruency method in a future publication.

### 4.1. *Shadow Detection With Image Gradients*

In the gradient method of edge detection, our aim is to generate an image not of the specific intensity of the source $I(\alpha,\beta)$, where $\alpha$ and $\beta$ are Cartesian coordinate on the observer's sky, but rather of the magnitude of the gradient of the specific intensity $|\nabla I(\alpha,\beta)|$. By construction, the image of the magnitude of the gradient will have local maxima at the locations of the steepest gradients, which, in the case of the expected EHT images, will coincide with the outline of the back hole shadow.

The magnitude of the gradient of the specific intensity is given by

$$|\nabla I(\alpha,\beta)| = \left[\left(\frac{\partial I}{\partial \alpha}\right)^2 + \left(\frac{\partial I}{\partial \beta}\right)^2\right]^{1/2} . \qquad (5)$$

For an image reconstructed from interferometric observations, each partial derivative can be easily calculated from the complex visibilities $V(u,v)$ using the van Cittert-Zernike theorem as, e.g.,

$$\frac{\partial I}{\partial \alpha} = \frac{2\pi i}{\lambda}\int du \int dv\, u V(u,v) e^{2\pi i(\alpha u+\beta v)/\lambda} . \qquad (6)$$

The above equations show that, in principle, generating a gradient image requires adding in quadrature two images constructed after multiplying first the complex visibilities by $iu$ and $iv$, respectively. In practice, the construction of a gradient image requires special care since the gradient operator in the $u-v$ plane will amplify the measurement errors in the largest baselines. This can be mitigated by designing an optimal high-frequency filter that will suppress the noise without unnecessarily sacrificing resolution. Moreover, the image reconstruction techniques that will be used need to employ priors that do not penalize narrow features, as is commonly done (see, e.g., Berger et al. 2012). In this paper, we consider only the principles of this approach, assuming no uncertainties and perfect coverage of the $u-v$ plane. In a follow-up paper, we will address the issues related to applying this approach to realistic EHT data.

Figure 5 shows the magnitude of the gradient of the accretion flow image shown in Figure 4 on the two-dimensional image plane of a distant observer as well as along three cross sections delineated by dashed lines. As expected, the steepest gradients and hence the brightest points in the gradient image occur at the rim of the black-hole shadow, with a notable exception near the equatorial plane (see also Figure 4). A second, fainter and larger rim appears at the outer edge of the image.

Having obtained a gradient image in which the rim of the black-hole shadow appears as the most discernible feature, we can now employ a pattern matching algorithm in order to determine the shape and size of the shadow. we will explore here the Hough transform (Duda & Hard 1972) and, in particular, we will follow the spirit of the closely connected Radon transform that allows for a probabilistic description of its results. This is crucial for our purposes because not only do we want an algorithm to measure the properties of the black-hole shadow but we also want to assess the statistical significance of the results.

As discussed earlier, in General Relativity, the outline of the black-hole shadow depends on only two parameters: the black-hole spin and the inclination of the observer. In principle, we can extract both these parameters using the pattern matching technique outlined below. In practice, however, the shape and size of the shadow has a very weak dependence on these parameters ($\pm 4\%$, see, e.g., Takahashi 2004; Bozza et al. 2006; Johannsen 2013). Moreover, the uncertainties in the prior knowledge of the astrophysical complexities discussed in the previous section are comparable to or larger than the range of shadow sizes predicted for the Kerr metric. As a result, we will primarily be able to test whether the properties of the shadow agree with the General Relativistic predictions and the Kerr metric rather than measure the spin of the black hole and the orientation of the observer. This is why we consider this approach a general relativistic null hypothesis test.

### 4.2. *Shadow Pattern Matching with the Hough/Radon Transform*

The Hough transform is a pattern matching technique used in computer vision to extract the properties of parametric curves based on an incomplete set of measurements of their outlines (Duda & Hard 1972). It is usually applied to a processed image, in which edges have been enhanced, as is the case of the gradient image discussed above.

If we denote by $\alpha$ and $\beta$ the two Cartesian coordinates on the image plane of a distant observer and, without lack of generality, assume that the $\alpha$ axis is parallel to the E-W direction and pointing towards the East, then the goal of the Hough transform is to identify the parameters of all curves of the form

$$\mathcal{C}(\alpha,\beta;\vec{M}) = 0 \qquad (7)$$

that best match the edge structures of the image. In this

expression, we used the vector $\vec{M}$ to denote the collection of parameters that are necessary to describe each curve. For convenience, we will also denote the gradient image by

$$\mathcal{G}(\alpha,\beta) \equiv |\nabla I(\alpha,\beta)| \ . \tag{8}$$

In the traditional Hough transform (albeit generalized to allow for curves that are not simply line segments), one generates the Hough accumulators (or Hough histograms) for each set of model parameters by counting all the pixels on the gradient image that lie along the corresponding curve for which the magnitude of the gradient is larger than a threshold, which we will call $G_0$. In other words, the Hough accumulators are

$$\mathcal{H}(\vec{M}) = \sum_{\alpha,\beta} \begin{cases} 1, & \text{if } \mathcal{C}(\alpha,\beta,\vec{M}) = 0 \text{ and } G(\alpha,\beta) > G_0 \\ 0, & \text{otherwise} \end{cases} \tag{9}$$

We can trivially generalize this definition to non pixelized images by making use of the $\delta$- and the Heaviside functions ($H$) such that

$$\mathcal{R}(\vec{M}) = \int d\alpha \int d\beta \delta \left[\mathcal{C}(\alpha,\beta,\vec{M})\right] H\left[G(\alpha,\beta) - G_0\right] \ . \tag{10}$$

This last expression is the Radon transform, which is closely related to the Hough transform and allows for a probabilistic description of the result in terms of possible Bayesian priors (see, e.g., Pereira Vasconcelos 2003; Bonci et al. 2005). In understanding the results of the Radon transform, special care needs to be taken in addressing the effects of incomplete sampling and discretization of the gradient image (see discussion in Pereira Vasconcelos 2003 and references therein).

In order to apply the Hough/Radon transform (10), we need a functional form for the shape of the black-hole shadow in terms of the model parameters. In General Relativity and for the Schwarzschild metric, the shape of the black-hole shadow is a circle. For the Kerr metric, the shape of the shadow is known in the form of a parametric analytic equation that, as expected, depends on only two quantities: the black-hole spin $a$ and the inclination of the observer $\theta_{\rm o}$ (Bardeen 1973; Chandrasekhar 1983). If we denote by $\alpha'$ and $\beta'$ two orthogonal angular coordinates on the image plane of a distant observer with $\alpha'$ perpendicular to the spin axis of the black hole, the parametric form of the shadow can be written as

$$\begin{aligned} \alpha'(r) &= -m \frac{\left[a^2(r+1) + (r-3)r^2\right] \csc\theta_{\rm o}}{a(r-1)} \\ \beta'_{\pm}(r) &= \pm m \frac{1}{a(r-1)} \left\{a^4 (r-1)^2 \cos^2\theta_{\rm o} \right. \\ &\quad + a(r-1)\left[a^2(r+1) + (r-3)r^2\right] \cot^2\theta_{\rm o} \\ &\quad \left. - r^3\left[(r-3)^2 r - 4a^2\right]\right\}^{1/2} \ . \end{aligned} \tag{11}$$

(Note some typos in Bardeen 1973, which were corrected in Chandrasekhar 1983). In these equations, the angular coordinates have been normalized to the opening angle of one gravitational radius of a black hole of mass $M_{\rm BH}$ positioned at a distance $D$ away from the observer, i.e., for

$$m \equiv \left(\frac{G M_{\rm BH}}{D c^2}\right) \ . \tag{12}$$

This is the quantity for which we have prior knowledge for Sgr A$^*$, as discussed in §2.

The parameter $r$, which corresponds to the coordinate radii of the orbits of the critical trajectories in units of $M_{\rm BH}$, takes values in the range $r_{ph-} < r < r_{\rm ph+}$ where $r_{\rm ph\pm}$ are the coordinate radii of the corotating and counter rotating equatorial photon orbits, i.e.,

$$r_{\rm ph\pm} = 2\left\{1 + \cos\left[\frac{2}{3}\cos^{-1}\left(\pm a\right)\right]\right\} \ . \tag{13}$$

Of course, the primed coordinate system, which is centered on the black hole, need not be centered on or aligned with the coordinate system on the image plane of the observer. If we denote by $\alpha_0$ and $\beta_0$ the horizontal and vertical displacements between the origins of the two coordinate systems and by $\phi$ the angle of rotation between the two frames (measured in degrees N of E) then the parametric form of the rim of the black-hole shadow on the coordinate system of the observer becomes

$$\begin{aligned} \alpha(r) &= \alpha_0 + \alpha'(r)\cos\phi + \beta'_{\pm}(r)\sin\phi \\ \beta_{\pm}(r) &= \beta_0 + \alpha'(r)\sin\phi + \beta'_{\pm}(r)\cos\phi \ . \end{aligned} \tag{14}$$

We can now use this parametric form in order to convert the surface integral of the Hough/Radon transform (10) to a contour integral over the parametric curve as

$$\begin{aligned} \mathcal{R}(\alpha_0,\beta_0,\phi,m,a) &= C \int_{r_{\rm ph-}}^{r_{\rm ph+}} dr \frac{ds}{dr} \\ &\quad \left\{H\left[G(\alpha,\beta_+) - G_0\right] + H\left[G(\alpha,\beta_-) - G_0\right]\right\} \ , \end{aligned} \tag{15}$$

where the expression for the derivative of the path length with respect to the parameter $r$, i.e.,

$$\frac{ds}{dr} \equiv \left[\left(\frac{d\alpha}{dr}\right)^2 + \left(\frac{d\beta}{dr}\right)^2\right]^{1/2} \tag{16}$$

is given in Appendix B. Of course, the contour integral along a curve will be proportional to its circumference. In order not to apply different weights to curves that have different circumferences, we have also normalized the Radon transform by the circumference of each curve, i.e.,

$$C^{-1} \equiv \int_{r_{\rm ph-}}^{r_{\rm ph+}} \left[\left(\frac{d\alpha}{dr}\right)^2 + \left(\frac{d\beta}{dr}\right)^2\right]^{1/2} dr \ . \tag{17}$$

The Radon transform evaluated for each set of model parameters measures the fractional length along the circumference of each curve on which the gradient has a magnitude larger than the prescribed threshold.

Naturally, this is not the only choice for the transform. If we have a measure of the statistical uncertainty $\sigma_{\rm G}$ in the measurement of each gradient, we can replace the Heaviside function with the posterior likelihood that a particular measurement is significant, i.e., with the error function, as

$$\begin{aligned} \mathcal{R}(\alpha_0,\beta_0,\phi,m,a) &= C \int_{r_{\rm ph-}}^{r_{\rm ph+}} dr \frac{ds}{dr} \\ &\quad \left\{\mathrm{erf}\left[\frac{G(\alpha,\beta_+)}{\sqrt{2}\sigma_{\rm G}}\right] + \mathrm{erf}\left[\frac{G(\alpha,\beta_-)}{\sqrt{2}\sigma_{\rm G}}\right]\right\} \ . \end{aligned} \tag{18}$$

Finally, given that we expect the black-hole shadow to generate the strongest gradients in the intensity of the image, we can introduce an additional weight to the Radon transform as

$$\mathcal{R}(\alpha_0,\beta_0,\phi,m,a) = C\int_{r_{\rm ph-}}^{r_{\rm ph+}} dr\frac{ds}{dr} \left\{G(\alpha,\beta_+){\rm erf}\left[\frac{G(\alpha,\beta_+)}{\sqrt{2}\sigma_{\rm G}}\right] + G(\alpha,\beta_-){\rm erf}\left[\frac{G(\alpha,\beta_-)}{\sqrt{2}\sigma_{\rm G}}\right]\right\} . \quad (19)$$

Each of these definitions have different strengths but also lead to Radon transforms that obey very different statistics.

It is important to emphasize here that the interferometric measurements of the gradients across the image will not be uncorrelated and will not obey simple Gaussian statistics. Indeed, given that the measurements are performed in the $u-v$ plane, all inferred gradients in the image plane will be highly correlated. Such correlations are not detrimental to our pattern matching algorithm, which only requires identifying the largest, statistically significant gradients on the image plane and does not depend strongly on the actual value or uncertainty of each gradient. Nevertheless, identifying the optimal definition of the Hough/Radon transform for our purposes and exploring its statistical properties is necessary and can be done within the context of mock simulated observations. This is beyond the scope of the current work and will be explored in a future article.

The parametric expressions (14) for the black-hole shadow are valid only for non-zero values of the black-hole spin. In the special case of a Schwarzschild black hole, the rim of the shadow is a circle with an apparent radius of $3\sqrt{3}m$, independent of the orientation of the observer. In order to account for this special case, we also need a different expression for the Radon transform. The parametric equation for rim of the shadow on the image plane of the observer become

$$\alpha(\Omega) = \alpha_0 + 3\sqrt{3}m\cos\Omega \quad (20)$$

$$\beta_\pm(\Omega) = \beta_0 \pm 3\sqrt{3}m\sin\Omega\,, \quad (21)$$

with $0 \le \Omega < \pi$. The Radon transform, in this case, then simply becomes a function of the three model parameters

$$\mathcal{R}(\alpha_0,\beta_0,m) = \frac{1}{2\pi}\int_0^\pi d\Omega \left\{H\left[G(\alpha,\beta_+)-G_0\right] + H\left[G(\alpha,\beta_-)-G_0\right]\right\}, \quad (22)$$

For the examples in this paper, we will use this last version of the Radon transform, i.e., assuming that the size of the black-hole shadow is always circular and equal to that of a Schwarzschild black hole. This is justified given the weak dependence of the black-hole size on black-hole spin and observer inclination (see, e.g., Chan et al. 2013) and the approximations regarding the observations that we will employ below. It is worth emphasizing, however, that there is no inherent difficulty in employing the complete form of the Radon transform and marginalizing over the spin of the black hole and the inclination of the observer.

The Hough/Radon transform (22) is a three-dimensional function of the model parameters $\alpha_0$, $\beta_0$, and $m$. Two of them are nuisance parameters (the coordinates of the center of the image), whereas the third parameter $m$ is the one of interest. The top panel of Figure 6 shows a cross section of the three-dimensional Hough/Radon transform for the gradient image of Figure 5. The vertical dashed line corresponds to the known opening angle (in units of $GM/Dc^2$) of the black-hole shadow.

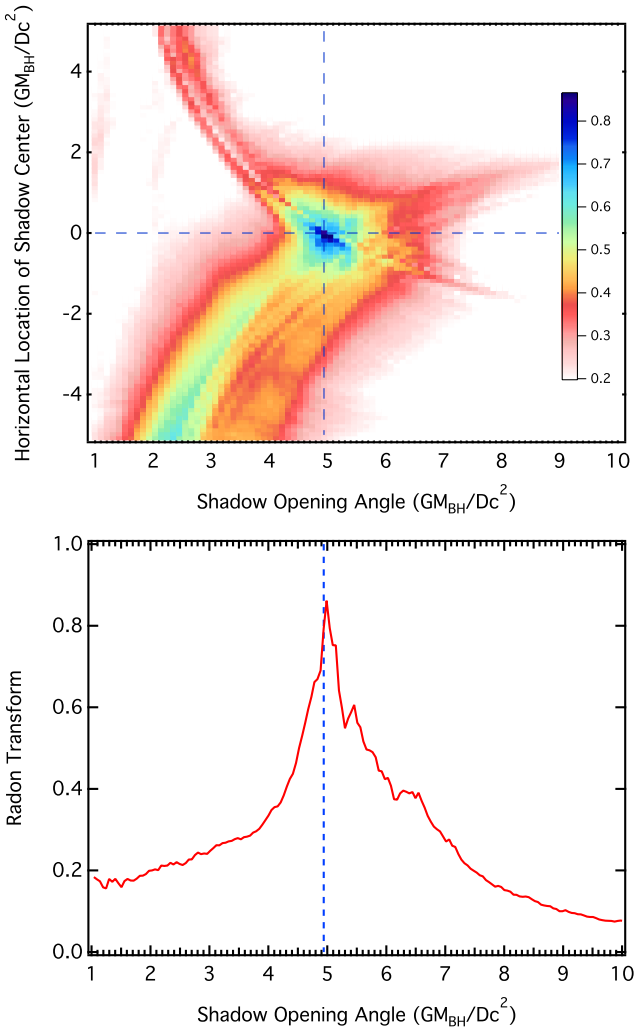
Horizontal Location of Shadow Center (GM_BH/Dc^2)
Shadow Opening Angle (GM_BH/Dc^2)
Radon Transform
Shadow Opening Angle (GM_BH/Dc^2)

FIG. 6.— *(Top)* A two dimensional cross section of the Radon transform of the image shown in Figure 4 on the plane of the parameter space that comprises the opening angle of the shadow and the horizontal location of the center of the black-hole shadow when the vertical location of the center of the shadow is set to zero ($\beta_0 = 0$). *(Bottom)* A cross section of the Radon transform for black-hole shadows centered at the known location of the black hole shadow. The narrow prominent peak is centered at the expected opening angle for the simulated black hole, shown as a vertical dashed line, and has a fractional HWHM of 9%. In both panels, all quantities are normalized to the ratio $GM_{\rm BH}/Dc^2$.

The bottom panel of Figure 6 shows the Hough/Radon transform, along a cross section of the parameter space that corresponds to $\alpha_0 = \beta_0 = 0$, i.e., for curves centered at the known center of the black-hole shadow. The peak occurs at the expected size of the black-hole shadow and its HWHM is approximately equal to 9%. This is the limiting accuracy with which the sharp gradient at the rim of the shadow can be localized, based on the most likely properties of the plasma emission in the vicinity of

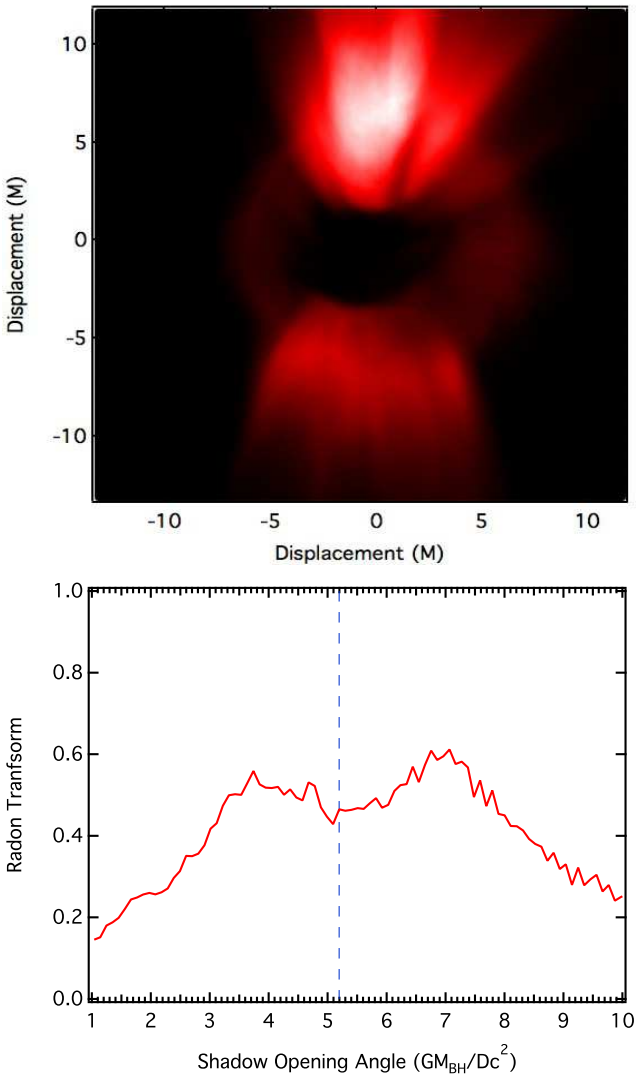


FIG. 7.— *(Top)* The simulated image for a MAD accretion flow around Sgr A* (aOMAD simulation in Chan et al. 2015a). This image is dominated by emission from the footpoints of the jets and shows only a very weak black-hole shadow. *(Bottom)* A cross section of the Radon transform for this image, for a pattern centered at the known location of the black hole shadow. When the emission pattern, or other astrophysical complications, do now allow for a signficant fraction of the black-hole shadow to become prominant, the Radon transform is inconclusive and does not lead to a biased measurement of the shadow properties.

Sgr A*, as inferred from our GRMHD simulations.

The particular simulation that we have used in the previous example shows a prominent shadow that shapes the brightness distribution of the images of the accretion flow. Is is possible, of course, that the images are dominated instead by bright spots with very weak evidence for the sharp gradients at the rim of the black-hole shadow. This is true, e.g., for images dominated by emission at the footpoints of jets, as in the simulations of Moscibrodzka et al. (2014) and the MAD simulations of Chan et al. (2015a), or at the standing shocks of tilted accretion disks, as in the simulations of Dexter & Fragile (2013). Alternatively, the intervening plasma might be blocking partially or fully the shadow and/or other structures, such as gravitationally lensed images of sheared flux tubes (see, e.g., Figure 9 of Chan et al. 2015b), might be mistaken for the shadow outline. In the latter case, such structures would be very short lived and repeated applications of the technique discussed here to images observed at different epochs should be able to filter against them. In the former case, however, it is important to show that the Radon transform of the gradient image will not lead to a biased measurement of the shadow properties.

The Radon transform becomes highly peaked only if sharp image gradients appear along a significant fraction of the pattern that is searched for. If the image shows shallower gradients along patterns that do not follow the expected outline of a Kerr shadow, then the Radon transform will not lead to a statistically significant measurement. To demonstrate this, Figure 7 shows the time-averaged image of the aOMAD simulation of Chan et al. (2015a), which is dominated by emission at the footpoints of the jet. The Radon transform of the gradient image in this case is very broad and inconclusive on whether the black-hole shadow has been detected or not. Determining the properties of the shadow from an image such as the one shown in this figure would be very challenging. Nevertheless, the advantage of the Radon transform is that it does not pick an erroneous value for the opening angle of the shadow but simply remains inconclusive. Astrophysical complexities might prohibit but will not bias a null hypothesis test of general relativity, as the one we discuss here.

## 5. CONCLUSIONS

The anticipated EHT observations of the black-hole shadow in Sgr A* will provide some of the strongest astrophysical evidence for the existence of black holes in the Universe and a direct observation of the effects of strong-field gravitational lensing. In this paper, we explored the prospect of performing a *qualitative* test of General Relativity using these observations in a manner that does not depend on the complex modeling of the accretion flow. In particular, we investigated the prospect of verifying the General Relativistic prediction for the half opening angle of the black-hole shadow in the Kerr metric, which is expected to be within 4% of $5GM/Dc^2$, for all black-hole spins and orientations of the distant observer.

Performing this null-hypothesis test requires four distinct steps. First, the theoretical prediction for the linear size of the black-hole shadow needs to be converted to an angular size on the observer's sky. This requires prior knowledge of the mass-to-distance ratio for Sgr A*, which is currently known to an adequate accuracy ($\sim 4\%$) from monitoring of stellar orbits. Future observations with next generation adaptive optics in 30-m class telescopes will reduce this uncertainty to less than one part in a thousand (Weinberg et al. 2005), effectively removing it from the error budget of the test.

Second, the blurring effects of scattering in the turbulent interstellar medium need to be removed in order for the sharp black-hole shadow to be easily distinguishable from the surrounding emission. Current observations suggest that the measurements of the scattering kernel need to be performed at large wavelengths (10-20 cm) and then extrapolated down to the 1.3 mm wavelength of EHT observations. Even though current measurements of the properties of the scattering ellipse at $10 - 20$ cm

are accurate to $3-20\%$, extrapolating them requires a theoretical model for the wavelength dependence of scattering induced blurring in anisotropic turbulence. This is the most severe current theoretical limitation in the null hypothesis test of General Relativistic that we propose here.

Third, the rim of the black hole shadow needs to be identified in the interferometric images, in a manner that does not depend on our prior knowledge and modeling of the accretion flow. We explored here an edge detection algorithm that identifies the black-hole shadow with the location of the sharpest gradients in the brightness image. Similar algorithms based on phase congruency are also likely to be applicable. Applying such algorithms directly to EHT data requires a detailed study of the statistics of the measured gradients, which will be highly correlated and non Gaussian.

Fourth, a pattern matching algorithm needs to be applied to the gradient images that will measure the properties of the black-hole shadow and in particular its opening angle. To this end, we investigated a variant of the Hough/Radon transform and applied it to mock images calculated from GRMHD simulations that have been tuned to match all current observations of Sgr A*. We found that, if Sgr A* behaves according to the most detailed currently available numerical models, then the Hough/Radon transform can lead to measurements of the opening angle of the black-hole shadow with an accuracy that is $\lesssim 10\%$.

Our main goal in this work has been to explore the principles of performing this quantitative null hypothesis test of General Relativity with EHT observations of Sgr A*. Our results now warrant a more detailed investigation of the practical application of our approach, considering the sparse sampling of the interferometric $u-v$ plane, the correlated uncertainties in the measurements, and the characteristic of the image reconstruction algorithms that will be used. We will explore these in a forthcoming article.

We thank Andrea Ghez, Sylvana Yelda, and Stefan Gillessen for providing us with their measurements of the mass and distance to Sgr A* based on the monitoring of stellar orbits. DP, FO, and CC were partially supported by NASA TCAN award NNX14AB48G. DP and CC also acknowledge support from NSF grant AST 1312034. FO ackowledges support from the Miller Institute for Basic Research at UC Berkeley. DM acknowledges support from NSF grant AST-1207752. All ray tracing calculations were performed with the `El Gato` GPU cluster at the University of Arizona that is funded by NSF award 1228509.

## APPENDIX

### A. A BAYESIAN ANALYSIS OF THE PROPERTIES OF THE SCATTERING SCREEN

In our investigation of the properties of the scattering screen towards Sgr A*, we faced the problem of combining measurements that are not necessarily in statistical agreement with each other. Such measurements suggest the presence of systematic unertainties that have not been accounted for in their error budget. If these systematic uncertainties are unaccounted for, they will lead to a significant underestimate of the final uncertainties of the properties of the scattering screen. In this appendix, we present a Bayesian analysis based on our earlier work (Güver et al. 2012a, 2012b) that allows us to quantify the degree of systematic uncertainties in an ensemble of measurements.

We will assume that each measurement of a quantity $f$ in the ensemle is drawn from a Gaussian distribution with a centroid at $f_0$ and a dispersion $\sigma$, i.e.,

$$P(f;f_0,\sigma) = C\exp\left[-\frac{(f-f_0)^2}{2\sigma^2}\right] , \tag{A1}$$

where $C$ is a proper normalization constant. This distribution is our model for the underlying systematic uncertainties in the measurements. Our goal is to calculate the posterior likelihood for the parameters $f_0$ and $\sigma$, $P(f_0,\sigma|\text{data})$, given an ensemble of $N$ measurements. Each of the measurements $f_i$, is described by a posterior likelihood, which we will assume here to be also a Gaussian with a centroid $f_{0,i}$ and a disperssion $\sigma_i$ i.e.,

$$P_i(f|f_{0,i},\sigma_i) = C_i\exp\left[-\frac{(f-f_{0,i})^2}{2\sigma_i^2}\right] , \tag{A2}$$

where $C_i$ is a set of normalization constants.

Using Bayes' theorem, we can write

$$P(f_0,\sigma|\text{data}) = C_0 P(\text{data}|f_0,\sigma)P(f_0)P(\sigma) . \tag{A3}$$

Here $C_0$ is a normalization constant, and $P(f_0)$ and $P(\sigma)$ are the priors over the centroid and dispersion of the underlying Gaussian distribution, which we take to be flat in a range larger than the anticipated values. Figure (3) shows that the $1-$ and $2-\sigma$ contours for the centroids of the three parameters of interest are quite narrow and, therefore, different broad prior distributions would have a very small effect on the final results. The range of statistically allowed dispersions, on the other hand, are larger and, therefore, are more susceptible to the properties of the prior distribution. When additional data are incorporated in this analysis to improve the statistics of the measured parameters, the effect of different priors will need to be investigated more thoroughly.

The quantity $P(\text{data}|f_0,\sigma)$ measures the likelihood that we will make a particular set of measurements given the values of the parameters of the underlying Gaussian distribution. Assuming for simplicity that these measurements

are uncorrelated, we write

$$P(\mathrm{data}|f_0,\sigma) = \prod_i \int df P_i(f|f_{0,i},\sigma_i) P(f;f_0,\sigma) \ . \tag{A4}$$

Inserting equation (A4) into equation (A3) we obtain the sought after posterior likelihood

$$P(f_0,\sigma|\mathrm{data}) = C_0 P(f_0) P(\sigma) \prod_i \int df P_i(f|f_{0,i},\sigma_i) P(f;f_0,\sigma) \ , \tag{A5}$$

where $C_0$ is an overall normalization constant.

Finally, in order to compute the posterior likelihood for the quantity $f$ given the two dimensional posterior likelihood of the centroid value $f_0$ and dispersion $\sigma$ of the underlying Gaussian distribution, we write

$$P(f) = \int\int P(f;f_0,\sigma) P(f_0,\sigma|\mathrm{data}) df_0 d\sigma \ . \tag{A6}$$

## B. THE CONTOUR INTEGRAL IN THE RADON TRANSFORM

In the calculation of the Radon transform using a parametric curve for the black-hole shadow, we need the derivative of the path length along the rim of the black-hole shadow and the parameter $r$. For a Kerr black hole, this is given by

$$\frac{ds}{dr} = \frac{r\left(r^2-3r+3\right)-a^2}{a(r-1)^2} \left\{ \frac{\left[a(r-1)\cot^2\theta_{\rm o} - 2(r-3)r^2\right]^2}{a^4(r-1)^2\cos^2\theta_{\rm o} + a(r-1)\left[a^2(r+1)+(r-3)r^2\right]\cot^2\theta_{\rm o} - r^3\left[(r-3)^2 r - 4a^2\right]} + 4\csc^2\theta_{\rm o} \right\}^{1/2} \ . \tag{B1}$$

## REFERENCES


Amarilla, L., & Eiroa, E. F. 2013, Phys. Rev. D, 87, 044057
Akiyama, K., Takahashi, R., Honma, M., Oyama, T., & Kobayashi, H. 2013, PASJ, 65, 91
Alberdi, A., Lara, L., Marcaide, J. M., et al. 1993, A&A, 277, L1
An, T., Goss, W. M., Zhao, J.-H., et al. 2005, ApJ, 634, L49
Bambi, C., & Yoshida, N. 2010, Classical and Quantum Gravity, 27, 205006
Bambi, C., & Freese, K. 2009, Phys. Rev. D, 79, 043002
Bardeen, J. M., Press, W. H., & Teukolsky, S. A. 1972, ApJ, 178, 347
Bardeen, J. M. 1973, Black Holes (Les Astres Occlus), 215
Berger, J.-P., Malbet, F., Baron, F., et al. 2012, A&A Rev., 20, 53
Boehle, et al. 2015, submitted
Bonci, A., Leo, T., & Longhi, S. 2005, IEEE Trans. Sys. Man. Cyb., A 35, 945
Bower, G. C., Falcke, H., Herrnstein, R. M., et al. 2004, Science, 304, 704
Bower, G. C., Goss, W. M., Falcke, H., Backer, D. C., & Lithwick, Y. 2006, ApJ, 648, L127
Bower, G. C., Markoff, S., Brunthaler, A., et al. 2014, ApJ, 790, 1
Bozza, V., de Luca, F., & Scarpetta, G. 2006, Phys. Rev. D, 74, 063001
Broderick, A. E., Fish, V. L., Doeleman, S. S., & Loeb, A. 2009, ApJ, 697, 45
Broderick, A. E., Fish, V. L., Doeleman, S. S., & Loeb, A. 2011, ApJ, 735, 110
Canny, J. F. 1983, M.Sc. Thesis, Massachusetts Inst. of Tech. Report, 720
Chan, C.-k., Psaltis, D., Özel, F. 2013, ApJ, 777, 13
Chan, C.-K., Psaltis, D., Ozel, F., Narayan, R., & Sadowski, A. 2015a, ApJ, 799, 1
Chan, C.-k., Psaltis, D., Ozel, F., et al. 2015b, ApJ, in press, arXiv:1505.01500
Chandran, B. D. G., & Backer, D. C. 2002, ApJ, 576, 176
Chandrasekhar, S. 1983, The Mathematical Theory of Black Holes, Oxford/New York, Clarendon Press/Oxford University Press (International Series of Monographs on Physics. Volume 69)
de Vries, A. 2000, Classical and Quantum Gravity, 17, 123
Dexter, J., Agol, E., & Fragile, P. C. 2009, ApJ, 703, L142
Dexter, J., Agol, E., Fragile, P. C., & McKinney, J. C. 2010, ApJ, 717, 1092
Dexter, J., & Fragile, P. C. 2013, MNRAS, 432, 2252
Doeleman, S. S., Weintroub, J., Rogers, A. E. E., et al. 2008, Nature, 455, 78
Duda, R. O. & Hard, P. E. 1972, Communications of the ACM, 15, 11
Eisenhauer, F., Perrin, G., Brandner, W., et al. 2011, The Messenger, 143, 16
Falcke, H., & Markoff, S. B. 2013, Classical and Quantum Gravity, 30, 244003
Falcke, H., Melia, F., & Agol, E. 2000, ApJ, 528, L13
Fish, V. L., Broderick, A. E., Doeleman, S. S., & Loeb, A. 2009, ApJ, 692, L14
Fish, V. L., Johnson, M. D., Lu, R.-S., et al. 2014, ApJ, 795, 134
Gaensler, B. M., Haverkorn, M., Burkhart, B., et al. 2011, Nature, 478, 214
Ghez, A. M., Salim, S., Weinberg, N. N., et al. 2008, ApJ, 689, 1044
Gillessen, S., Eisenhauer, F., Fritz, T. K., et al. 2009a, ApJ, 707, L114
Gillessen, S., Eisenhauer, F., Trippe, S., et al. 2009b, ApJ, 692, 1075
Goodman, J., & Narayan, R. 1989, MNRAS, 238, 995
Güver, T., Psaltis, D., Özel, F. 2012a, ApJ, 747, 76
Güver, T., Özel, F., & Psaltis, D. 2012b, ApJ, 747, 77
Gwinn, C. R., Kovalev, Y. Y., Johnson, M. D., & Soglasnov, V. A. 2014, ApJ, 794, LL14
Jaroszynski, M., & Kurpiewski, A. 1997, A&A, 326, 419
Jauncey, D. L., Tzioumis, A. K., Preston, R. A., et al. 1989, AJ, 98, 44
Johannsen, T. 2013, Phys. Rev. D, 87, 124017
Johannsen, T., & Psaltis, D. 2010, ApJ, 718, 446
Johnson, M. D., & Gwinn, C. R. 2015, ApJ, 805, 180
Kovesi, P. D. 1999, Journal of Computer Vision Research 1
Liu, K., Wex, N., Kramer, M., Cordes, J. M., & Lazio, T. J. W. 2012, ApJ, 747, 1
Lo, K. Y., Backer, D. C., Kellermann, K. I., et al. 1993, Nature, 362, 38
Lo, K. Y., Backer, D. C., Ekers, R. D., et al. 1985, Nature, 315, 124
Lu, R.-S., Krichbaum, T. P., Eckart, A., et al. 2011, A&A, 525, A76
Luminet, J.-P. 1979, A&A, 75, 228

Marcaide, J. M., Alberdi, A., Lara, L., Pérez-Torres, M. A., & Diamond, P. J. 1999, A&A, 343, 801
Marr, D., & Hildreth, E. 1980, Royal Society of London Proceedings Series B, 207, 187
Mościbrodzka, M., Gammie, C. F., Dolence, J. C., Shiokawa, H., & Leung, P. K. 2009, ApJ, 706, 497
Mościbrodzka, M., & Falcke, H. 2013, A&A, 559, LL3
Mościbrodzka, M., Falcke, H., Shiokawa, H., & Gammie, C. F. 2014, A&A, 570, AA7
Narayan, R., & Goodman, J. 1989, MNRAS, 238, 963
Özel, F., Psaltis, D., & Narayan, R. 2000, ApJ, 541, 234
Pereira Vasconcelos, M. A.,S. 2003, Ph.D. Thesis, Harvard University
Pfahl, E., & Loeb, A. 2004, ApJ, 615, 253
Psaltis, D., Narayan, R., Fish, V. L., et al. 2015a, ApJ, 798, 15
Psaltis, D., Wex, N., & Kramer, M. 2015b, ApJ, in press
Roy, S., & Pramesh Rao, A. 2003, Astronomische Nachrichten Supplement, 324, 391
Shen, Z.-Q., Lo, K. Y., Liang, M.-C., Ho, P. T. P., & Zhao, J.-H. 2005, Nature, 438, 62
Takahashi, R. 2004, ApJ, 611, 996
Weinberg, N. N., Milosavljević, M., & Ghez, A. M. 2005, ApJ, 622, 878
Yusef-Zadeh, F., Cotton, W., Wardle, M., Melia, F., & Roberts, D. A. 1994, ApJ, 434, L63